nature electronics

Article

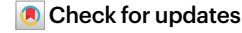
https://doi.org/10.1038/s41928-024-01195-z

A polymer-semiconductor-ceramic cantilever for high-sensitivity fluid-compatible microelectromechanical systems

Received: 21 June 2023

Accepted: 30 May 2024

Published online: 15 July 2024



Dear Prof. Brugger, the text highlighted in yellow are about the fabrication itself and in light purple about the general concept and the device itself. We have merged the supplementary material to this file as well since more details on the fabrication and the process flow is shown there (page 13 of this file)

Thank you in advance for your time!

Nahid Hosseini © ^{1,5}, Matthias Neuenschwander © ^{1,5}, Jonathan D. Adams © ¹, Santiago H. Andany ¹, Oliver Peric ¹, Marcel Winhold ², Maria Carmen Giordano © ³, Vinayak Shantaram Bhat ³, Marcos Penedo © ¹, Dirk Grundler © ^{3,4} & Georg E. Fantner © ¹ \bowtie

Active microelectromechanical systems (MEMS) with integrated electronic sensing and actuation can provide fast and sensitive measurements of force, acceleration and biological analytes. Strain sensors integrated onto MEMS cantilevers are widely used to transduce an applied force to an electrical signal in applications like atomic force microscopy and molecular detection. However, the high Young's moduli of traditional MEMS materials, such as silicon or silicon nitride, limit the thickness of the devices and, therefore, the deflection sensitivity that can be obtained for a specific spring constant. Here, we show that polymer materials with a low Young's modulus can be integrated into polymer-semiconductor-ceramic MEMS cantilevers that are thick and soft. We develop a multi-layer fabrication approach so that high-temperature processes can be used for the deposition and doping of piezoresistive semiconductor strain sensors without damaging the polymer layer. Our trilayer cantilever exhibits a sixfold reduction in force noise compared to a comparable self-sensing silicon cantilever. Furthermore, the strain-sensing electronics in our system are embedded between the polymer and ceramic layers, which makes the technology fluid-compatible.

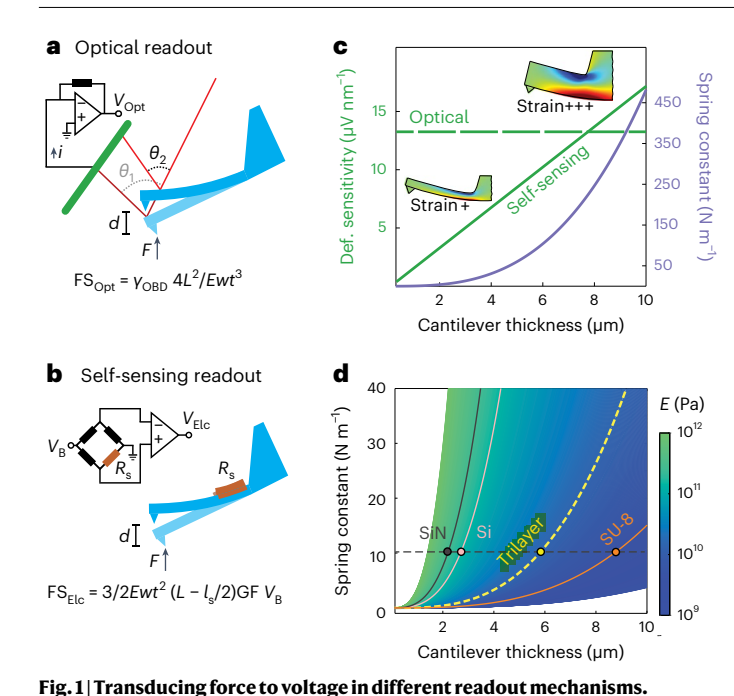
Self-sensing cantilevers

Microelectromechanical systems (MEMS) are regularly used in sensing applications. MEMS cantilevers are, in particular, used in atomic force microscopy (AFM) to probe samples in the nanoscale regime. Traditionally, the deflection of an AFM cantilever is detected using the optical beam deflection (OBD) method¹ in which a laser beam is reflected from the back of the cantilever and centred on a quadrant photodiode (Fig. 1a). Cantilevers with integrated sensing elements that can self-sense their deflection have also been developed²-8. These are usually made of traditional MEMS materials (silicon or silicon nitride910) and feature a piezoresistive strain sensor near their fixed end (Fig. 1b).

However, they have not found widespread use in AFM because of their lower force sensitivity (FS) and signal-to-noise ratio compared to optically detected cantilevers.

The difference in FS between optical and piezoelectric sensing is a consequence of the different quantities being measured. OBD measures the change in angle of the cantilever at its free end, whereas self-sensing cantilevers measure the strain in the base of the cantilever. The FS achievable depends on the deflection sensitivity (DS) of the readout method and the cantilever spring constant (k) as FS = DS/k. The deflection angle does not depend on the thickness of the

¹Laboratory for Bio- and Nano-Instrumentation, Interfaculty Institute of Bioengineering, École Polytechnique Fédérale de Lausanne (EPFL), Lausanne, Switzerland. ²GETec Microscopy GmbH, Vienna, Austria. ³Laboratory of Nanoscale Magnetic Materials and Magnonics, Institute of Materials, Ecole Polytechnique Fédérale de Lausanne (EPFL), Lausanne, Switzerland. ⁴Institute of Electrical and Micro Engineering, Ecole Polytechnique Fédérale de Lausanne (EPFL), Lausanne, Switzerland. ⁵These authors contributed equally: Nahid Hosseini, Matthias Neuenschwander. ⊠e-mail: georg.fantner@epfl.ch



a, Optical scheme. The applied force causes a deflection of the cantilever, which

consequently changes the spot position of the reflected laser beam on the quadrant photodiode. The force sensitivity (FS_{Opt}) is defined as V_{Opt}/F , where L, w, t and E are the length, width, thickness and Young's modulus of the cantilever, respectively. All parameters that are independent of the cantilever mechanics are combined in one constant y_{OBD} . **b**, Self-sensing scheme. The applied force causes a deflection that induces a strain at the base of the cantilever. A piezoresistive sensor is integrated at the upper surface of the cantilever. The resistance R_s is measured by a Wheatstone bridge and subsequent readout electronics. The self-sensing force sensitivity (FS_{E1c} = $3/2Ewt^2(L - l_s/2)$ GF V_B) depends on the gauge factor (GF) of the sensing element, the bridge bias voltage (V_B) , the cantilever dimensions and the piezoresistor length (l_s) . \mathbf{c} , The DS of the optical scheme (V_{Opt}/d) is independent of cantilever thickness. The self-sensing DS $(V_{\rm Ele}/{\rm d})$ increases for larger cantilever thicknesses. Insets, A given deflection will induce a higher strain in a thick cantilever, as shown by the finite element analysis. The DS was simulated for a 150 μ m \times 50 μ m cantilever footprint and a Wheatstone bridge with a bias voltage of 2 V. The spring constant of the cantilever, however, increased with the cube of the thickness. d, The spring constant also depends on the material's Young's modulus. Soft materials like polymers show the same spring constant for larger thicknesses than conventional MEMS materials (for example, silicon and silicon nitride). The dashed line represents the spring constant of trilayer cantilevers with a footprint size of 150 μ m \times 50 μ m.

Why to use polymers as the core material?

cantilever, and therefore, the DS for the OBD method is independent of the cantilever thickness (Fig. 1c and Supplementary Information Note 1). In contrast, for self-sensing cantilevers, the DS increases with cantilever thickness (Fig. 1c and Supplementary Information Note 2). Therefore, a thicker cantilever exhibits a higher DS¹¹. However, thicker cantilevers also have a higher spring constant. To achieve high FS, the thickness of the cantilever must increase without increasing the spring constant.

Polymers have much lower Young's moduli. The Young's modulus of SU-8 is, for example, around 60 times lower than that of silicon nitride. This allows polymer MEMS to have thicker cantilevers while maintaining a low spring constant (Fig. 1d). Polymer MEMS are attractive for AFM applications 12-14 and can be combined with other materials for strain sensing^{15–21}. However, the gauge factors of compatible materials are generally much lower than those of semiconductor strain sensors, so the advantage of increased cantilever thickness is offset by lower strain sensor performance. On the other hand, the high temperature required to deposit semiconductors to achieve strain gauges with high gauge factors are incompatible with polymer materials.

In this article, we report a MEMS microfabrication platform that can be used to create polymer cantilevers with integrated semiconductor electronics. This allows the cantilevers to be thick and soft, so that we can achieve high DS and FS. We use high-performance electronics for sensing and actuation. The cantilever consists of a polymer core sandwiched between two ceramic silicon nitride layers to form a trilayer structure. The semiconductor sensing electronics are embedded between the polymer and one of the hard ceramic layers. Crucially, in the fabrication method, the high-temperature processes needed to make the electronics are separated from the polymer processes needed to make the cantilever core.

Our trilayer cantilevers show six times lower force noise compared to silicon cantilevers. Furthermore, by incorporating the sensing electronics inside the polymer MEMS, they are isolated from the environment. This makes the cantilevers inherently fluid-compatible and means that the cantilever tip side can have multifunctional coatings. We show that the polymer-semiconductor-ceramic cantilever can be used in self-sensing AFM and in membrane surface-stress sensors used to detect biomolecules. Even in a harsh fluidic environment (ferric chloride), the trilayer cantilever can image for 5 h without showing signs of degradation.

Concept and performance of the trilayer cantilever

Figure 2a shows a schematic of the structure of a self-sensing AFM cantilever made with our process for fabricating a hybrid polymer-semiconductor-ceramic cantilever. We used a polymer as the main structural component to obtain thick yet soft cantilevers. The strain-sensing elements are integrated away from the neutral axis to maximize the DS. The polymer core is enveloped by two hard thin film layers (Fig. 2a), which optimizes the transmission of strain from the core to the strain sensors²². In this trilayer structure, the active electronic parts are embedded between the polymer and the hard ceramic layer, and hence, they are isolated from the environment. This makes the cantilevers inherently fluid-compatible, and means that a cantilever's tip side can have multifunctional coatings, which is an established technique for conventional OBD cantilevers. The fabrication of the trilayer cantilevers (Fig. 2b and Supplementary Information Note 3) is based on polymer bonding of two preprocessed wafers, each containing one of the ceramic thin films. The high-temperature processes required to fabricate the sensing elements are performed on one or both wafers before wafer bonding. The wafers are then spin-coated and bonded using the polymer benzocyclobutene (BCB). The devices are released by etching silicon through the wafer with potassium hydroxide (KOH) and dry etching the trilayer structure. This results in a trilayer cantilever on a silicon chip, such that the sensing elements and electrical connections are hermetically sealed inside the hard films (Fig. 2b). We chose BCB as the core material for our trilayer devices because it is a widely used polymer for wafer bonding that can be easily deposited through spin coating, can be dry etched with standard reactive ion etching chemistry and has excellent chemical properties. However, other bonding materials could also be considered with slight changes to the microfabrication process, such as polyimide or parylene-N.

The trilayer design provides additional degrees of freedom to optimize the performance of the MEMS cantilever. In traditional single-layer cantilevers, only the thickness and planar dimensions can be tuned to obtain a particular MEMS device. In the trilateral devices, the thickness of the BCB core, the thickness of the hard thin film and the material of the thin film can be tuned to optimize the mechanical and electrical performance of the cantilever. The influence of these three factors can be approximated by a structural mechanics model that calculates the expected DS, spring constant and FS of the cantilevers (Supplementary Information Note 2). Figure 3a presents the theoretical curves for the DS, spring constant, and FS of trilayer cantilevers for different thicknesses of the BCB core. These cantilevers have

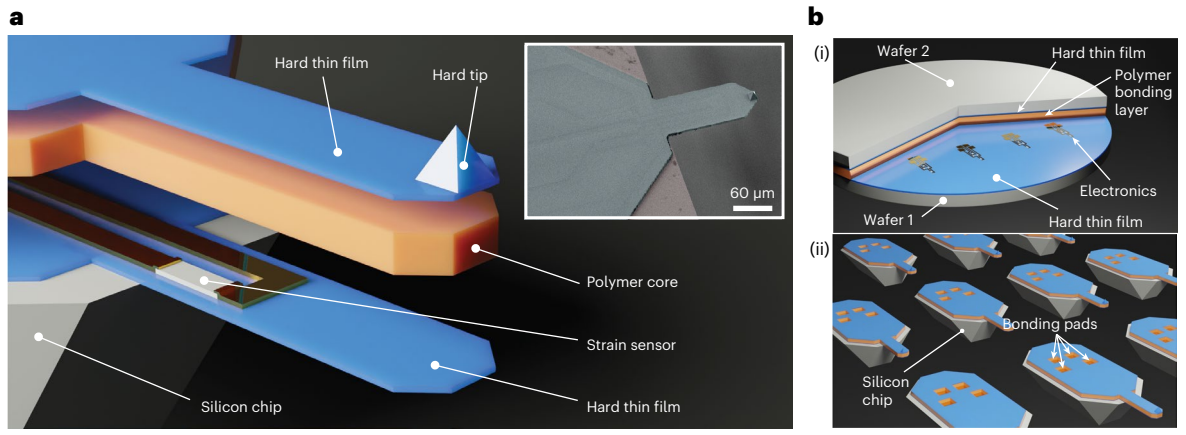


Fig. 2 | **Trilayer cantilever concept and performance.** *a*, Schematic of the trilayer cantilever illustrating the polymer core and self-sensing electronics sandwiched between two hard thin films. Due to the polymer core, the cantilever can be thick while having a low spring constant. The DS increases if the sensing element is placed further away from the neutral axis. Inset, SEM image of a trilayer cantilever. The sensing elements are buried under the hard thin film.

b, The fabrication process is based on polymer bonding of two processed wafers. Each wafer is coated with a thin film of silicon nitride (blue) with the same thickness. BCB (orange) is spin-coated onto one wafer, and piezoresistors and metallic interconnections are patterned onto the other. The two wafers are then bonded together. Silicon chip bodies (grey) are made by etching silicon with potassium hydroxide (KOH).

a footprint of 150 μ m \times 50 μ m. They have a polysilicon strain sensor and two 20 nm low-stress silicon nitride films as the hard outer layers. Two cantilevers were fabricated with these parameters with BCB layer thicknesses of 1.6 and 3.2 μ m. Our experimental results matched the predicted values very well without any parameter fitting (circular points in Fig. 3a). Using the same model, we compared the theoretical FS of various versions of trilayer cantilevers with typical single-crystal silicon cantilevers. Figure 3b shows that the known general trend of increased FS for decreased thicknesses remains true. However, for a given cantilever thickness, the FS of the trilayer cantilevers is up to ten times higher than that of silicon cantilevers. In very thin cantilevers, the FS advantage of the trilayer cantilevers over silicon cantilevers is less pronounced, because the relative stiffness contribution of the polymer decreases compared to the contribution of the silicon nitride.

An inherent advantage of our trilayer process is that it enables production of polymer-core cantilevers with strain sensors that possess the same high gauge factor as sensors used in silicon cantilevers. Notably, our trilayer and silicon cantilevers achieved equivalent gauge factors and voltage noise levels by utilizing identical readout electronics. Consequently, the trilayer cantilevers exhibit comparable noise levels while delivering superior FS compared to silicon levers. We compared both technologies experimentally by measuring the force noise spectra of two cantilevers with equal dimensions (330 μm long, 110 μm wide and 3.2 µm thick) based on single-crystal silicon piezoresistors, both arranged in a Wheatstone bridge configuration (Fig. 3c). The trilayer cantilever has a six times better force noise compared to the silicon cantilever. The high DS and FS allow low-noise AFM measurements of a highly ordered pyrolytic graphite surface. The Z noise level was 0.4 Å (Fig. 3d), and the 3.4 Å atomic steps are clearly visible (Fig. 3e). Using the trilayer structure, we were able to increase the FS over conventional silicon self-sensing cantilevers by a factor of 6. Whether the FS of the trilayer cantilever outperforms that of OBD cantilevers depends on the desired cantilever spring constant, which is generally given by the application and dynamic force range.

High tracking bandwidth of amplitude-modulation AFM

In addition to the increased sensitivity, the polymer core of the trilayer cantilever also improves the imaging speed in amplitude-modulation (AM) tapping mode. The bandwidth of a cantilever in AM mode is a measure of the maximum rate of topography change the cantilever can accurately detect. The bandwidth scales with f_0/Q , where f_0 is the

cantilever's resonance frequency and Q is its mechanical quality factor (Q-factor)²³. We previously showed that making cantilevers from the polymer SU-8 greatly increases the achievable imaging speed because of the high internal damping and inherently low Q-factor¹². The same effect is observed for the trilayer cantilevers because the damping is dominated by the polymer core. This is particularly advantageous when imaging in vacuum, because the absence of fluid or air damping causes the Q-factor to be dominated by the internal damping of the material. We, therefore, compared the imaging speeds achievable with silicon and trilayer cantilevers in a combined AFM and scanning electron microscope (SEM) system (Fig. 4). We imaged the same sample (a wasp eye) with two cantilevers of similar resonance frequency and size using the same AFM (Methods) installed inside a SEM (Fig. 4a,b). The SEM image shows the closely packed ommatidium lens surfaces of the wasp eye. The AFM image shows the nano-nipple arrays on the cornea of one ommatidium²⁴ imaged using a trilayer and a silicon cantilever at 2 lines per second and 32 lines per second (Fig. 4b). Although the silicon cantilever tracks the nanostructures poorly at a scan rate of 32 lines per second, the trilayer cantilever detects the sample topography much better due to its lower Q-factor.

Fluid and coating compatibility of the trilayer platform

All the sensing elements and electrical connections in the trilayer platform are hermetically sealed inside the MEMS device, which makes it inherently compatible with measurement applications in fluids. This is particularly important for biological measurements in life sciences, but also for operating the devices in opaque or harsh chemical environments. As a proof of principle, we imaged the etching process of a polished nickel surface in ferric chloride, a strongly corrosive opaque solution (Fig. 5a and Supplementary Video 1). Even after 5 h of imaging, the cantilever showed no signs of degradation.

In addition to imaging in liquids, the isolated sensing electronics make the trilayer cantilevers a versatile tool for other AFM modes, for example, those that require special coatings on the tip such as Kelvin probe force microscopy (KPFM) or magnetic force microscopy (MFM). Coating traditional self-sensing cantilevers can cause shorting of the self-sensing electrical connections unless additional passivation layers are applied^{25,26}. However, such passivation layers negatively affect the self-sensing performance and are prone to failure^{27,28}. Here, a conductive or magnetic coating can simply be applied through evaporation and sputtering, in the same way as for passive

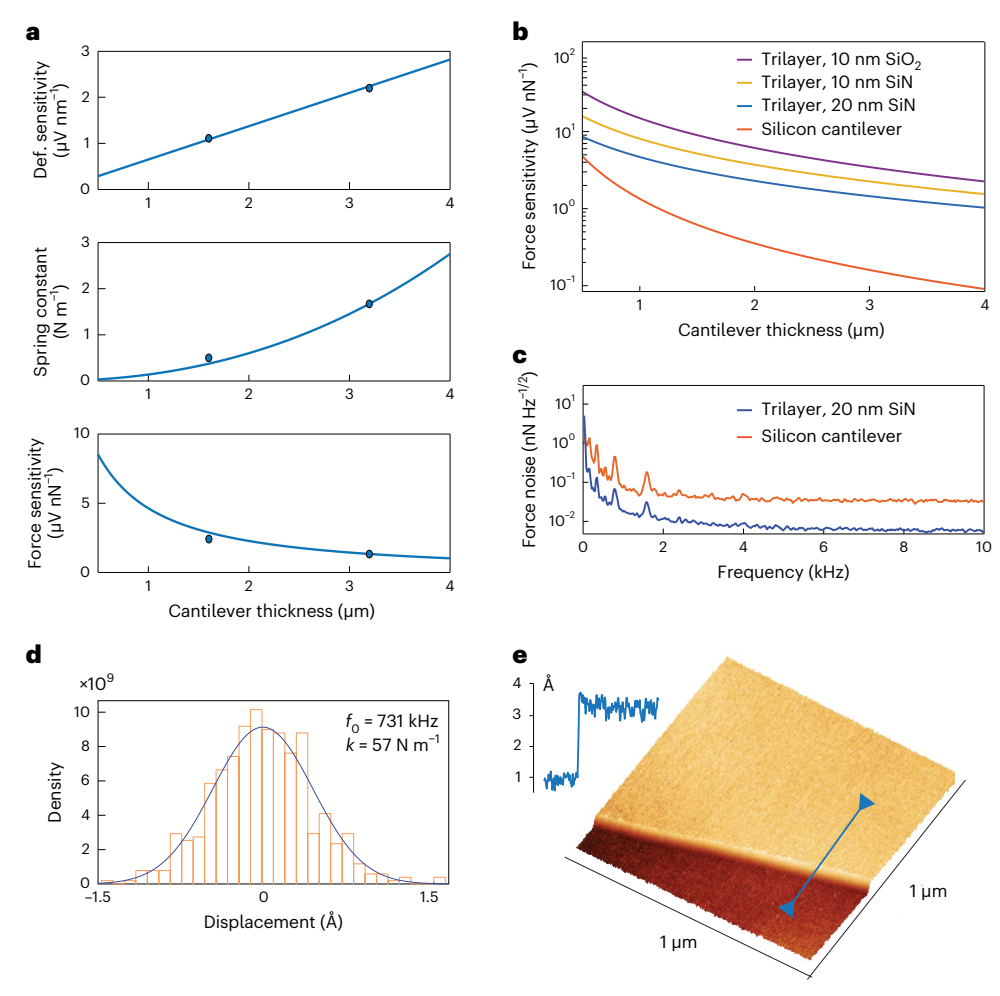
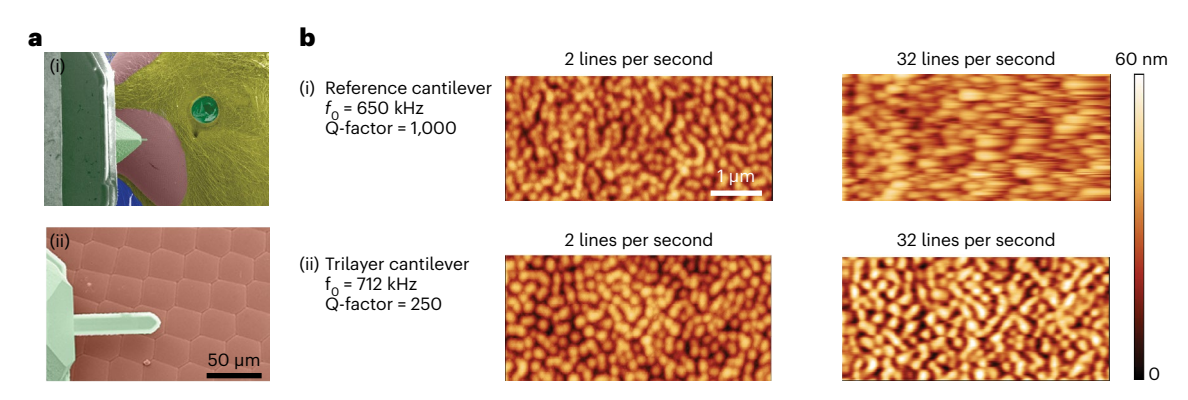


Fig. 3 | **Theoretical and experimental evaluation of the trilayer technology. a**, Calculated DS, spring constant and FS of the trilayer cantilever made with polysilicon piezoresistors. Circular points represent experimental data of two trilayer cantilevers with the same planar dimensions (150 μ m \times 50 μ m), silicon nitride layer thickness of 20 nm, and BCB thicknesses of 1.6 μ m and 3.2 μ m. The DS and the spring constant increased by increasing the thickness. The FS decreased for thicker cantilevers. **b**, Comparison between a monolithic silicon cantilever and the trilayer technology with different material combinations.

All cantilevers were assumed to have identical strain sensors. The cantilever footprint was 150 μ m × 50 μ m. **c**, Force noise measurements for a trilayer and silicon cantilever with similar dimensions and monocrystalline silicon piezoresistors. **d**, Due to the enhanced DS, the trilayer cantilever with integrated polysilicon piezoresistors in air (spring constant, k=57 N m $^{-1}$) had a root mean square noise value of 0.4 Å. **e**, AFM measurement of a single atomic layer of highly ordered pyrolytic graphite using the trilayer cantilever.



 $\label{eq:Fig.4} \textbf{High tracking bandwidth of trilayer cantilevers for AM-AFM in vacuum. a, (i) SEM image of the wasp eye investigated with an SEM-AFM hybrid system. (ii) SEM image of the cantilever and the closely packed ommatidia at the surface of the wasp eye. The SEM is used to navigate the cantilever on top of an ommatidium. b, An ommatidium surface imaged using a reference cantilever$

(i) and a trilayer cantilever (ii). The trilayer cantilever has a lower Q-factor and therefore higher detection bandwidth, allowing for greatly improved tracking when the image speed is increased to 32 lines per second. The colour scale bar represents the surface topography.

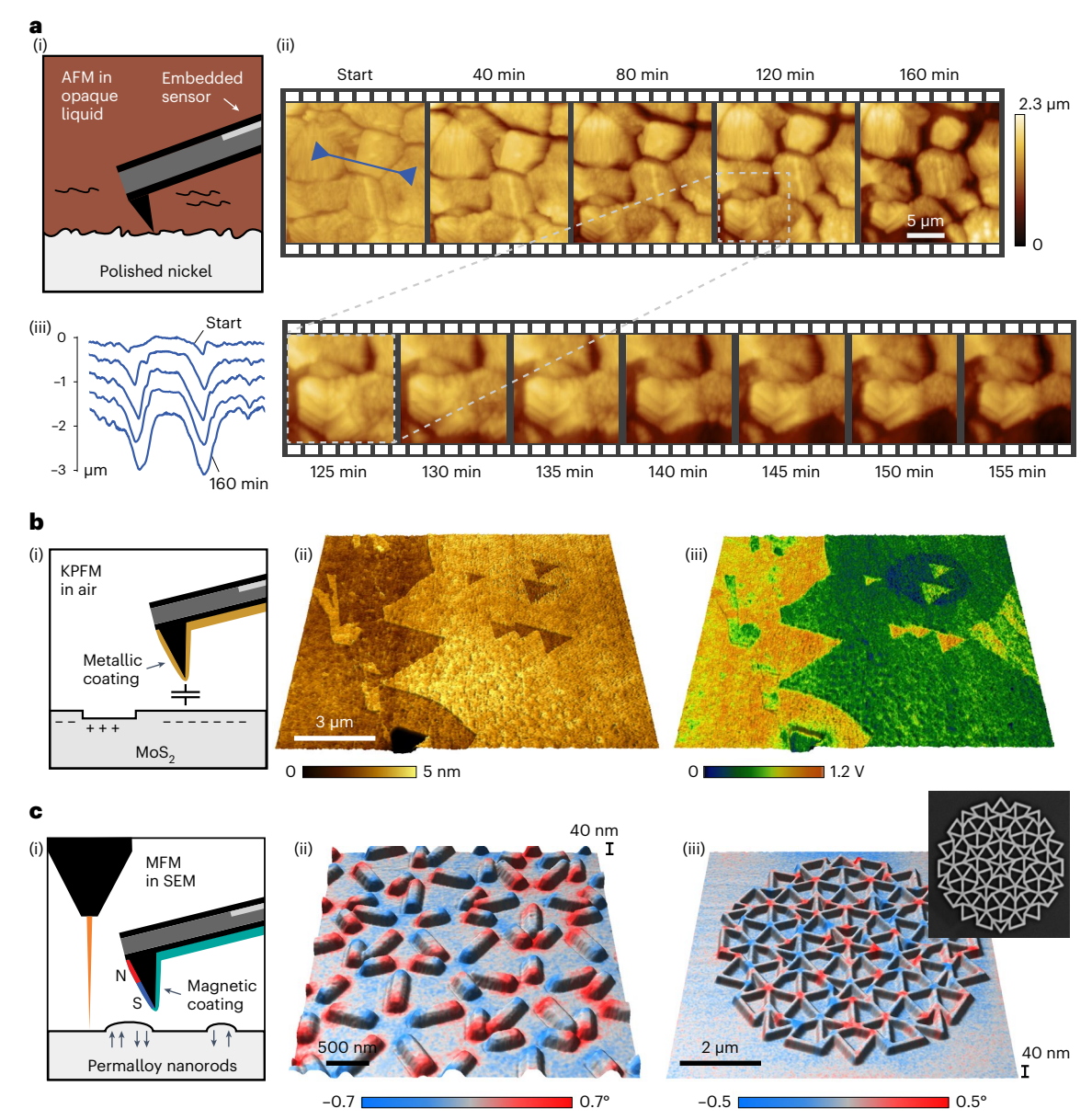


Fig. 5 | Trilayer cantilevers as a platform for various scanning probe techniques. a, (i) Diagram for AFM using a trilayer cantilever to investigate the evolution of a polished nickel surface when it is exposed to corrosive FeCl₃. (ii) 160 min time-lapse images showing the etching of nickel grains by FeCl₃. (iii) Line profiles taken at 0, 40, 80, 120 and 160 min showing how the grain boundaries evolve during etching. b, (i) Diagram showing a trilayer cantilever modified by coating the AFM tip with 100 nm of gold to make it conductive for KPFM applications. (ii) Sample topography of few-layered MoS₂ showing two distinct layers. (iii) Superposition of topography and work function revealing

the surface potential difference between the layers. \mathbf{c} , (i) Diagram showing a trilayer cantilever modified for MFM measurements by coating the AFM tip with 70 nm of Ni $_{\rm sl}$ Fe $_{\rm l9}$. Measurements were performed in a vacuum with a hybrid SEM-AFM system. (ii) Superposition of topography and phase data showing the intensity of the magnetic field created by separated Ni $_{\rm sl}$ Fe $_{\rm l9}$ nanorods. (iii) The same technique applied to interconnected Ni $_{\rm sl}$ Fe $_{\rm l9}$ nanorods on a rotationally symmetric quasicrystal lattice. The colour scale bar displays the phase shift of the oscillating cantilever as it passes over the sample surface. Inset, SEM image of the nanorod structure.

optical cantilevers. This enables KPFM and MFM measurements with self-sensing cantilevers. KPFM relies on measuring the potential difference between a conductive tip and the sample surface, which creates a surface work function map. We performed frequency-modulation self-sensing KPFM on few-layered molybdenum disulfide (MoS₂), revealing the sample topography and its surface potential simultaneously (Fig. 5b). MFM measurements require a magnetic coating on the AFM cantilever tip. We evaporated 70 nm of Ni₈₁Fe₁₉ onto trilayer cantilevers and obtained correlated SEM, AFM and MFM images of interconnected and disconnected networks of Ni₈₁Fe₁₉ nanorods patterned onto fivefold rotationally symmetric Penrose P2 quasicrystal lattices (Fig. 5c). Such structures, in which each nanorod essentially

functions as a small ferromagnet, are candidates for ultra-high-density data storage²⁹. The MFM data reveal that the intensity of the magnetic field, displayed in red and blue, is different at each of the vertices. The vertices with high intensity act as hotspots where ferromagnetic switching of the nanorods will begin under an applied magnetic field³⁰. The permalloy-coated, self-sensing cantilever enabled seamless SEM/AFM/MFM correlative imaging.

The trilayer technology is not limited to self-sensing cantilevers. We fabricated fluid-compatible membrane-type surface-stress sensors³¹ (Fig. 6a) using the same technology. Such sensors feature a large membrane suspended by four bridges that contain strain sensors. The membrane can be functionalized to detect different gases

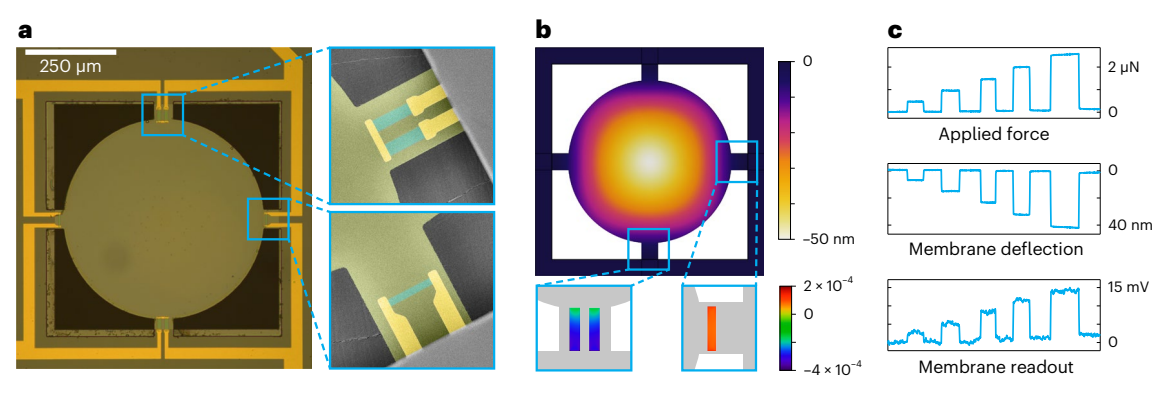


Fig. 6 | Trilayer MEMS for fluid-proof membrane surface-stress sensing.

a, A trilayer membrane with a diameter of 500 μ m is suspended by four beams with integrated piezoresistive sensors. In two beams, the resistors are parallel, and in the other two beams they are transverse (inset images). b, Finite element analysis shows that when a point force is applied at the centre of the membrane, there is a negative resistive change in the parallel piezoresistors and a positive

change in the transverse resistors. The colour scale bars show the membrane's relative deflection and resistive changes due to the applied force. \mathbf{c} , Force was applied to the centre of the membrane using an AFM cantilever, which induced a deflection. The resistive change of the piezoresistors was detected with a full Wheatstone bridge readout.

or specific molecules. Upon exposure to the target entity, the membrane is subject to surface stress, which is amplified in the suspension bridges and detected by the strain sensors there. Here, we performed a proof-of-concept experiment during which we applied a force at the centre of the membrane using an AFM cantilever. Simulations show that for a 2 μN force, a membrane deflection of 50 nm was expected, along with resistive changes of -4×10^{-4} and 2×10^{-4} for the parallel and transverse sensors, respectively (Fig. 6b). The experimental results confirm these findings (Fig. 6c). As trilayer devices are inherently fluid-compatible, these membranes could be used for biosensing in liquid for point-of-care diagnostics 32,33 .

Conclusions

Integrating self-sensing (and actuation) electronics into MEMS devices is typically achieved by depositing the electronic materials onto the main structural MEMS material. The advantage of this approach is that a range of standard microfabrication processes and materials are available. However, a problem with this approach is that the structural material must be able to withstand the often harsh processing conditions of the electronic materials. This means that polymers, and other more sensitive materials, cannot be used as the structural components of a MEMS device. We overcome this problem by separating the high-temperature processes for the electronic components from the polymer-based processes of the core MEMS material.

Our trilayer fabrication process has a number of advantages that make it a promising fabrication platform for advanced MEMS devices. First, the ability to use polymers as the main structural material extends the Young's modulus and density range for the MEMS body materials by orders of magnitude. This gives additional degrees of freedom for tuning the mechanical performance of the MEMS device and complements the traditional geometric optimization degrees of freedom. Second, the electronic elements are no longer on the exposed side of the MEMS device but sealed inside it. This is particularly beneficial for MEMS devices operating in harsh environments, liquids or complex biological fluids. Third, the process is inherently extendable, allowing for several planes of active electronic components inside a MEMS device (five, seven, nine, etc. layers, each individually electrically addressable).

The use of polymer materials as the main structural component for self-sensing MEMS can have advantages and disadvantages, depending on the application. The inherently low Q-factor of polymer-based MEMS devices is advantageous for dynamic AFM applications but is poorly suited for resonators used in mass sensing, where a high Q-factor is important for obtaining high sensitivity. Moreover, BCB has very different thermal properties (both thermal expansion and

thermal conductivity) than silicon nitride. A change in temperature will, therefore, lead to differential thermal expansion in the BCB and the silicon nitride, thereby inducing shear stress on the polymer/silicon nitride interface. Due to the symmetric nature of the trilayer structure, this shear stress is symmetric on the top and bottom interfaces, so that the cantilever will not deform substantially.

BCB wafer bonding leads to residual stress in the bonding interface³⁴. Stresses in double-sided clamped beams can strongly affect the resonance frequency of the beam³⁵. In single-sided clamped cantilever beams, the effect of residual stresses is, however, orders of magnitude smaller³⁶, which is probably why we have not observed any issues relating to the resonance frequency due to the residual stress. A change in temperature, however, could result in a change in resonance frequency due to the relative elongation of the cantilever and the potential softening of the BCB core. The glass transition temperature of BCB (350 °C) limits the temperature range over which the MEMS devices can be used. Excessive changes in temperature can change the mechanical properties of the device and, for example, shift the resonance frequency of the cantilevers. Device ageing is also a concern for polymer MEMS. Systematic ageing studies remain to be done, but we have not observed any excessive ageing, even for devices fabricated 4 yr ago.

Our trilayer fabrication approach has potential applications beyond improving the sensitivity of self-sensing MEMS devices. For example, at present, only simple piezoresistive strain gauges have been embedded into our devices. However, more complex electronics such as pre-amplification electronics, could be integrated into the platform because all processes for the electronic components occur before polymer bonding and shaping of the MEMS. The fabrication platform could allow the integration of actuators and sensing electronics, as well as bonding to wafers with complementary metal–oxide–semiconductor (CMOS)-based devices. The polymer itself could also be used to add functionality to the MEMS devices. For example, the BCB could be etched or photo-patterned³⁷ before the wafer bonding process to create microfluidic self-sensing MEMS devices.

Methods

Cantilever characterization

To calculate the cantilever properties presented in Fig. 3a,b, we used the following values for the Young's moduli: $E_{\rm LSNT}$ = 240 GPa, $E_{\rm BCB}$ = 2.9 GPa, $E_{\rm Silicon}$ = 130 GPa and $E_{\rm SiO2}$ = 66 GPa. Cantilever length 150 µm, width 50 µm and low-stress silicon nitride (LS-SiN) thickness 20 nm. The BCB thickness varied from 300 nm to 4 µm. The piezoresistor length, width and thickness were 40 µm, 8 µm and 100 nm respectively. The gauge factor of polysilicon was measured as 25.

The experimental data were taken using a controller (NanoscopeV, Bruker) and AFM system (MultiModeV, Bruker). The differential signal from the Wheatstone bridge was amplified with a low-noise instrumentation amplifier (AD8429, Analog Devices) and two operational amplifiers for a total gain of 1,000. The electronics output (deflection signal) was then fed into Bruker Signal Access Module III. The electrical DS for each individual cantilever was obtained in contact mode. The thermomechanical tuning was measured to characterize the resonance frequency and the spring constant of the cantilevers.

Noise measurement

The noise spectrum in Fig. 3c was acquired with a lock-in amplifier (UHF 600 MHz, 1.8 GSa $\rm s^{-1}$, Zurich Instruments) for a trilayer cantilever and a silicon cantilever (AMG Technology Ltd, Botevgrad, Bulgaria). Both cantilevers had integrated boron-doped silicon piezoresistors.

The AM-AFM noise in Fig. 3d was measured with the system described in Methods ('Cantilever characterization'). The scan size was set to a very small value (for example, 0.01 nm) and the feedback gain was reduced close to zero, so that there was no topography change and no tracking by the proportional–integral–derivative controller. All the fluctuations in the self-sensing deflection signal were contained in the amplitude error signal. The distribution of these fluctuations was used to compute the root mean square noise.

Measurements in vacuum

All the vacuum measurements were performed in a hybrid SEM-AFM system (GETec, moved to QD Microscopy) with a controller (Anfatec Instruments AG).

Nickel etching

The experiment was performed using a Bruker NanoscopeV controller and a Dimension Icon AFM scan head with a homebuilt, liquid-compatible cantilever holder. The electrical deflection signal was sent to the INO port of Bruker Signal Access Module III. The images were taken in PeakForce Tapping with a 50 nN force set point, 1 kHz peak-force frequency and 1 Hz scan rate.

KPFM

KPFM cantilevers were manufactured on a wafer-scale by evaporating a 100 nm gold layer onto them using a shadow mask. Evaporation was preferred over sputtering because it allowed accurate coverage, especially for the intended areas. A lock-in amplifier (UHFLI, Zurich Instruments) was used to implement the KPFM. The conductive tip of the cantilever was biased with 2.5 V at a frequency of 2 kHz. The cantilever oscillation amplitude at the side-band frequencies was detected and minimized by applying a DC offset voltage to the sample. Control was achieved with the proportional—integral—derivative controller of the lock-in amplifier. Images were taken with a Bruker NanoscopeV controller and MultiModeV AFM system in FM-KPFM.

MFM

Images were taken in a vacuum using the SEM-AFM hybrid system described in Methods. MFM trilayer cantilevers were made by depositing a 70 nm layer of nickel-iron alloy (permalloy) onto the cantilever tip using an evaporation process. To enhance the signal quality in MFM measurements, the cantilevers were positioned at an angle during deposition, thus ensuring the permalloy coating was on only one side (facing the clamped end) of the cantilever tip. Additionally, to prevent a short circuit between the piezoresistors, the bonding pads were protected during the deposition process.

AFM image processing

Images were processed in Gwyddion. We removed the line-by-line offset using a median correction method and subtracted the background tilt or bow using first- and second-order polynomial fittings. The nickel

etch images were cropped to compensate for the sample drift. Noise in the height images of KPFM and MFM was reduced with a 3-pixel median average filter.

Sample preparation

The wasp was found dead. Its head was removed and coated with gold and palladium to provide a conductive layer for SEM. The nickel surface was polished with silica suspensions (0.05 μm) in the Interdisciplinary Centre for Electron Microscopy at the Swiss Federal Institute of Technology in Lausanne (EPFL). The MFM sample was provided by D. Grunder (Laboratory of Nanoscale Magnetic Materials and Magnonics. EPFL).

Data availability

The data that support the findings of this study are available via Zenodo at https://doi.org/10.5281/zenodo.11198161 (ref. 38).

Code availability

The Matlab code used to generate plots is available via Zenodo at https://doi.org/10.5281/zenodo.11198347 (ref. 39).

References

- Meyer, G. & Amer, N. M. Novel optical approach to atomic force microscopy. Appl. Phys. Lett. 53, 1045–1047 (1988).
- Tortonese, M., Yamada, H., Barrett, R. C. & Quate, C. F. Atomic force microscopy using a piezoresistive cantilever. In TRANSDUCERS'91: 1991 International Conference on Solid-State Sensors and Actuators. Digest of Technical Papers 448–451 (IEEE. 1991): https://doi.org/10.1109/SENSOR.1991.148908
- Minne, S. C., Manalis, S. R. & Quate, C. F. Parallel atomic force microscopy using cantilevers with integrated piezoresistive sensors and integrated piezoelectric actuators. *Appl. Phys. Lett.* 67, 3918–3920 (1995).
- Watanabe, S. & Fujii, T. Micro-fabricated piezoelectric cantilever for atomic force microscopy. Rev. Sci. Instrum. 67, 3898–3903 (1996).
- 5. Harley, J. A. & Kenny, T. W. High-sensitivity piezoresistive cantilevers under 1000 Å thick. *Appl. Phys. Lett.* **75**, 289–291 (1999).
- Boisen, A., Thaysen, J., Jensenius, H. & Hansen, O. Environmental sensors based on micromachined cantilevers with integrated read-out. *Ultramicroscopy* 82, 11–16 (2000).
- Li, M., Tang, H. X. & Roukes, M. L. Ultra-sensitive NEMS-based cantilevers for sensing, scanned probe and very high-frequency applications. Nat. Nanotechnol. 2, 114–120 (2007).
- Tosolini, G., Scarponi, F., Cannistraro, S. & Bausells, J. Biomolecule recognition using piezoresistive nanomechanical force probes. Appl. Phys. Lett. 102, 253701 (2013).
- Nam, H. J. et al. Silicon nitride cantilever array integrated with silicon heaters and piezoelectric detectors for probe-based data storage. Sens. Actuators A: Phys. 134, 329–333 (2007).
- De Pastina, A., Maillard, D. & Villanueva, L. G. Fabrication of suspended microchannel resonators with integrated piezoelectric transduction. *Microelectron. Eng.* 192, 83–87 (2018).
- Dukic, M., Adams, J. D. & Fantner, G. E. Piezoresistive AFM cantilevers surpassing standard optical beam deflection in low noise topography imaging. Sci. Rep. 5, 16393 (2015).
- Adams, J. D., Fantner, G. E., Grossenbacher, J., Nievergelt, A. & Brugger, J. Harnessing the damping properties of materials for high-speed atomic force microscopy. *Nat. Nanotechnol.* 11, 147 (2016).
- Hosseini, N. et al. Batch fabrication of multilayer polymer cantilevers with integrated hard tips for high-speed atomic force microscopy. In 2019 20th International Conference on Solid-State Sensors, Actuators and Microsystems and Eurosensors XXXIII (TRANSDUCERS & EUROSENSORS XXXIII) 2033–2036 (IEEE, 2019); https://doi.org/10.1109/TRANSDUCERS.2019.8808606

- Hosseini, N., Neuenschwander, M., Peric, O., Andany, S.H., Adams, J.D. & Fantner, G.E. Integration of sharp silicon nitride tips into high-speed SU8 cantilevers in a batch fabrication process. Beilstein J. Nanotechnol. 10, 2357–2363 (2019).
- 15. Johansson, A., Calleja, M., Rasmussen, P. A. & Boisen, A. SU-8 cantilever sensor system with integrated readout. *Sens. Actuators A: Phys.* **123–124**, 111–115 (2005).
- Mathew, R. & Ravi Sankar, A. A review on surface stress-based miniaturized piezoresistive SU-8 polymeric cantilever sensors. Nano-Micro Lett. 10, 35 (2018).
- Tina, B. S., Anjana, C., Kumar, N. & Seena, V. Polymer/ceramic MEMS: a nanomechanical sensor platform with low temperature high gauge factor ITO for electromechanical transduction. J. Microelectromech. Syst. 30, 116–125 (2021).
- Kim, D.-S., Jeong, Y.-J., Park, J., Shanmugasundaram, A. & Lee, D.-W. Multi-layered polymer cantilever integrated with full-bridge strain sensor to enhance force sensitivity in cardiac contractility measurement. *Analyst* 146, 7160–7167 (2021).
- Nordström, M. et al. SU-8 cantilevers for bio/chemical sensing; fabrication, characterisation and development of novel read-out methods. Sensors 8, 1595–1612 (2008).
- Reddy, C. V. B. et al. Piezoresistive SU-8 cantilever with Fe(iii) porphyrin coating for CO sensing. *IEEE Trans. Nanotechnol.* 11, 701–706 (2012).
- Johansson, A., Blagoi, G. & Boisen, A. Polymeric cantileverbased biosensors with integrated readout. Appl. Phys. Lett. 89, 173505 (2006).
- Adams, J. D. et al. Analysis of local deformation effects in resistive strain sensing of a submicron-thickness AFM cantilever. In Proc. Smart Sensors, Actuators, and MEMS VI (eds Schmid, U. et al.) 876327 (International Society for Optics and Photonics, 2013).
- Mertz, J., Marti, O. & Mlynek, J. Regulation of a microcantilever response by force feedback. Appl. Phys. Lett. 62, 2344–2346 (1993).
- Kryuchkov, M. et al. Analysis of micro- and nano-structures of the corneal surface of *Drosophila* and its mutants by atomic force microscopy and optical diffraction. *PLoS ONE* 6, e22237 (2011).
- Gotszalk, T., Grabiec, P., Shi, F., Dumania, P., Hudek, P. & Rangelow, I. W. Fabrication of multipurpose AFM/SCM/SEP microprobe with integrated piezoresistive deflection sensor and isolated conductive tip. *Microelectron. Eng.* 41–42, 477–480 (1998).
- Harjee, N., Haemmerli, A., Goldhaber-Gordon, D. & Pruitt, B. L. Coaxial tip piezoresistive scanning probes with sub-nanometer vertical displacement resolution. In SENSORS, 2010 IEEE 1962– 1966 (IEEE, 2010); https://doi.org/10.1109/ICSENS.2010.5689882
- Villanueva, G., Plaza, J. A., Montserrat, J., Perez-Murano, F. & Bausells, J. Crystalline silicon cantilevers for piezoresistive detection of biomolecular forces. *Microelectron. Eng.* 85, 1120–1123 (2008).
- Doll, J. C. & Pruitt, B. L. High-bandwidth piezoresistive force probes with integrated thermal actuation. *J. Micromech. Microeng.* 22, 095012 (2012).
- 29. Weber, D. P. et al. Cantilever magnetometry of individual Ni nanotubes. *Nano Lett.* **12**, 6139–6144 (2012).
- Bhat, V. S. et al. Controlled magnetic reversal in permalloy films patterned into artificial quasicrystals. *Phys. Rev. Lett.* 111, 077201 (2013).
- Lang, H. P. et al. Piezoresistive membrane surface stress sensors for characterization of breath samples of head and neck cancer patients. Sensors 16, 1149 (2016).
- McKendry, R. et al. Multiple label-free biodetection and quantitative DNA-binding assays on a nanomechanical cantilever array. Proc. Natl Acad. Sci. USA 99, 9783–9788 (2002).
- Huber, F., Lang, H. P., Zhang, J., Rimoldi, D. & Gerber, C. Nanosensors for cancer detection. Swiss Med. Wkly 145, w14092 (2015).

- Weigel, P. O. & Mookherjea, S. Reducing the thermal stress in a heterogeneous material stack for large-area hybrid optical silicon-lithium niobate waveguide micro-chips. Opt. Mater. 66, 605–610 (2017).
- 35. Karabalin, R. B., Villanueva, L. G., Matheny, M. H., Sader, J. E. & Roukes, M. L. Stress-induced variations in the stiffness of microand nanocantilever beams. *Phys. Rev. Lett.* **108**, 236101 (2012).
- Lachut, M. J. & Sader, J. E. Effect of surface stress on the stiffness of cantilever plates. *Phys. Rev. Lett.* 99, 206102 (2007).
- Zhou, X., Virasawmy, S. & Quan, C. Wafer-level BCB bonding using a thermal press for microfluidics. *Microsyst. Technol.* 15, 573–580 (2009).
- Hosseini, N. Dataset and AMF images. Zenodo https://doi.org/ 10.5281/zenodo.11198161 (2024).
- 39. Hosseini, N. MATLAB codes to generate the plots. *Zenodo* https://doi.org/10.5281/zenodo.11198347 (2024).

Acknowledgements

We sincerely thank the Center of Micronanotechnology at EPFL for their invaluable assistance throughout the microfabrication process. We thank A. Kis and H. Ji from the Laboratory of Nanoscale Electronics and Structures at EPFL for graciously providing the ${\rm MoS_2}$ sample for the KPFM measurement. We gratefully acknowledge the financial support received from several sources. This includes European Union funding (Framework Programme FP7/2007-2013/ERC under Grant Agreement No. 307338-Eurostars El 8213-Triple-S), a consolidator grant from the European Research Council (ERC-2017-CoG) and the InCell project (Project No. 773091). We appreciate the financial support from the Swiss National Science Foundation under grant numbers SNSF 200021-182562, SNSF 200020-213072, and SNSF 205320-152675. Their generous support has been instrumental in completing this research. Our research on artificial Ni₈₁Fe₁₉ quasicrystals was funded by the Swiss National Science Foundation (Project No. 163016).

Author contributions

N.H. and M.N. developed the microfabrication process, fabricated the trilayer MEMS devices in the clean room, designed and performed the experiments, built the instrumentation, analysed the data and wrote the paper. J.D.A. developed the microfabrication process and fabricated the trilayer MEMS devices in the clean room. S.H.A. and O.P. fabricated the trilayer MEMS devices in the clean room. M.C.G., V.Sh.B. and D.G. provided support for the coating of MFM tips and the artificial Ni $_{81}$ Fe $_{19}$ quasicrystals used for the MFM studies. M.W. performed the SEM/AFM/MFM experiment. M.P. provided support for the KPFM application. G.E.F. coordinated the research, designed the experiments and wrote the paper.

Competing interests

The authors declare the following competing interests. J.D.A., G.E.F. and N.H. have a patent on the technology under Patent number WO2016189451A1.

Additional information

Supplementary information The online version contains supplementary material available at https://doi.org/10.1038/s41928-024-01195-z.

Correspondence and requests for materials should be addressed to Georg E. Fantner.

Peer review information *Nature Electronics* thanks Yonggang Jiang, Prosenjit Sen and Akanksha Singh and the other, anonymous, reviewer(s) for their contribution to the peer review of this work.

Reprints and permissions information is available at www.nature.com/reprints.

Publisher's note Springer Nature remains neutral with regard to jurisdictional claims in published maps and institutional affiliations.

Springer Nature or its licensor (e.g. a society or other partner) holds exclusive rights to this article under a publishing agreement with the author(s) or other rightsholder(s); author

self-archiving of the accepted manuscript version of this article is solely governed by the terms of such publishing agreement and applicable law.

@ The Author(s), under exclusive licence to Springer Nature Limited 2024

nature electronics

Supplementary information

https://doi.org/10.1038/s41928-024-01195-z

A polymer–semiconductor–ceramic cantilever for high-sensitivity fluid-compatible microelectromechanical systems

In the format provided by the authors and unedited

Supplementary information

Note 1- Optical readout deflection and force sensitivity

In the Optical Beam Deflection (OBD) method, a focused laser beam is illuminated onto the cantilever backside, and the reflected laser beam is detected with position-sensitive photodetectors (PSPD). A cantilever deflection d coming from a point force F acting on the cantilever free-end induces a bending angle $\Delta\theta$ along the cantilever length¹:

$$\Delta\theta = \frac{3}{2} \frac{d}{L} \tag{1}$$

where L is the cantilever length. The cantilever deflection d deflects the reflected laser beam by $2\Delta\theta$, which moves the laser beam with the spot area of $a \times a$ by Δa on the PSPD:

$$\Delta a = 3 \frac{L_{CP}}{I} d \tag{2}$$

where, L_{CP} is the distance between the cantilever's free end and the PSPD.

Initially, the laser spot is aligned to the center of the PSPD ($\Delta a = 0$), and each of the two photodiodes (top and bottom) produces an equal amount of current:

$$i_1 = i_2 = \frac{\eta P_0 \alpha}{2} \tag{3}$$

Where η , P_0 and α are the efficiency of the light-to-current conversion at the photodiode, the output power of the laser diode and the laser power attenuation coefficient in the optical path. The displacement of the laser spot results in a difference between the photo-induced currents from the two photodiodes. Assuming that the laser spot shape is rectangular and the power distribution is uniform, the current difference is given by:

$$\Delta i = i_1 - i_2 = \eta P_0 \alpha \frac{2\Delta a}{a} \tag{4}$$

The photo-induced differential current Δi from the PSPD is converted to a voltage signal V_{Opt} through a transimpedance preamplifier and a differential amplifier¹:

$$V_{opt} = 6 \eta \frac{P_0}{a} \alpha A_{diff} R_{IV} \frac{L_{CP}}{L} d$$
 (5)

Where R_{IV} and A_{diff} are the transimpedance of the preamplifier and the gain of the differential amplifier, respectively. Finally, a correction factor χ can be introduced to account for the fact that the laser spot is a Gaussian distribution rather than a square¹:

$$V_{opt} = 6 \eta \frac{P_0}{a} \alpha \chi A_{diff} R_{IV} \frac{L_{CP}}{L} d$$
 (6)

Therefore, the optical deflection sensitivity is given by:

$$DS_{opt} = \frac{V_{opt}}{d} = 6 \eta \frac{P_0 \alpha}{a} \chi A_{diff} R_{IV} \frac{L_{CP}}{L}$$
 (7)

For readability, all parameters that are independent of the cantilever mechanics can be combined in one constant γ_{OBD} :

$$DS_{Opt} = \gamma_{OBD} \frac{1}{I} \tag{8}$$

The force sensitivity (FS) is described as the induced output voltage divided by the applied force ($FS_{Opt} = V_{Opt}/F$), where the force is related to the deflection through the spring constant: F = kd. For a cantilever beam with a rectangular cross-section, made of a monolithic material with Young's modulus E, exposed to the force F at its free end:

$$k = \frac{3EI}{L^3} = \frac{Ewt^3}{4L^3} \tag{9}$$

where *t* and *w* are the cantilever thickness and width. Therefore:

$$FS_{Opt} = \gamma_{OBD} \frac{4L^2}{Ewt^3} \tag{10}$$

with

$$\gamma_{OBD} = 6 \, \eta \, \frac{P_0 \alpha}{a} \chi \, A_{diff} R_{IV} L_{CP} \tag{11}$$

Note 2- Self-sensing readout deflection and force sensitivity

To find the self-sensing deflection sensitivity, we calculate the longitudinal strain $\varepsilon(x,z)$ in the beam induced by a given deflection d:

$$\varepsilon(x,z) = \frac{M(x)}{EI_{eq}}z\tag{12}$$

where, M(x) = F(L - x) is the bending moment for an applied force F and EI_{eq} is the effective flexural rigidity of the beam. Using the expression for the spring constant and by assuming the piezoresistor has a thickness of t_s and length l_s and is placed at the surface of the cantilever with a thickness t:

$$\varepsilon\left(\frac{l_s}{2}, \frac{t}{2}\right) = \frac{3t}{2L^2} \left(1 - \frac{l_s}{2L}\right) d\tag{13}$$

For a Wheatstone bridge with one active resistor, the strain is converted to a voltage change defined by the gauge factor GF of the piezoresistors and the bridge supply voltage V_B :

$$V_{Elc} = \frac{\Delta R}{4R} V_B = \frac{GF \, \varepsilon \left(\frac{l_S \, t}{2 \, \prime 2}\right)}{4} V_B = \frac{3}{8} \frac{t}{L^2} \left(1 - \frac{l_S}{2L}\right) GF \, V_B d \tag{14}$$

finally, the deflection sensitivity ($DS_{Elc} = V_{Elc}/d$) and the force sensitivity ($FS_{Elc} = V_{Elc}/F$) are given by:

$$DS_{Elc} = \frac{3}{8} \frac{t}{L^2} \left(1 - \frac{l_s}{2L} \right) GF V_B \tag{15}$$

$$FS_{Elc} = \frac{1}{8} \frac{t}{EI_{eq}} \left(L - \frac{l_s}{2} \right) GF V_B$$
 (16)

For a cantilever beam with a rectangular cross-section, made of a monolithic material with the Young's modulus E, FS_{Elc} becomes:

$$FS_{Elc} = \frac{3}{2Ewt^2} \left(L - \frac{l_s}{2} \right) GF V_B \tag{17}$$

The sandwich beam theory is used to estimate the relevant properties of the trilayer piezoresistive cantilevers, including the force sensitivity, the resonance frequency and the spring constant. Figure S1 shows a sketch of the cross-section of the modeled beam.

The distance between the center line of film layers is calculated $d_m=t+f$, where E_{core} and t are Young's Modulus and the thickness of the cantilever core material. For a monolithic cantilever f=0

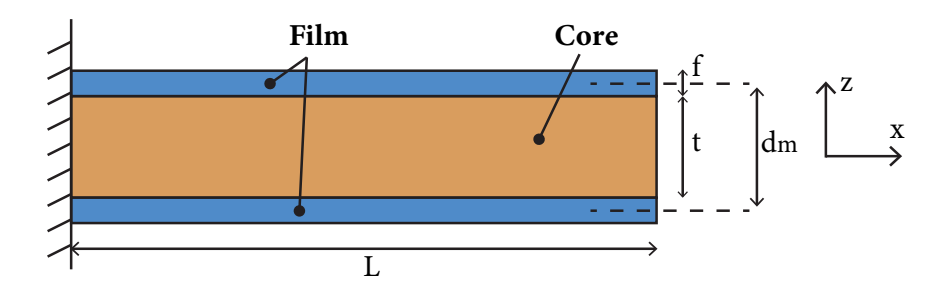


Figure S1. Cross-section of the modeled sandwich beam, showing the key dimensions. The width of the beam (w) is not shown

For a trilayer cantilever:

$$EI_{eq} = E_{film} \left(\frac{wf^3}{6} + \frac{wfd_m^2}{2} \right) + E_{core} \frac{wt^3}{12}$$
 (18)

Next, we calculate the mass per unit length of the cantilever. With ρ_{core} and ρ_{film} the densities of the core and film materials, we have:

$$m_{eq} = w(2f\rho_{film} + t\rho_{core}) \tag{19}$$

The spring constant and the resonant frequency of the trilayer beam are achieved by using:

$$k = \frac{3EI_{eq}}{L^3} \tag{20}$$

$$f_0 = \frac{0.56}{L^2} \sqrt{\frac{EI_{eq}}{m_{eq}}} \tag{21}$$

The force sensitivity is obtainable for a trilayer cantilever by replacing equation (20) in (16).

Note 3- Microfabrication process flow of the trilayer AFM cantilevers

The microfabrication process flow for the trilayer devices is described here.

S3-1 Electronics

S3-1-1 Polysilicon piezoresistor: The integrated electronics are fabricated first. This allows the use of high-temperature processes like LPCVD or diffusion before any polymer is introduced. First, low-stress silicon nitride (LS-SiN) with a minimum thickness of 20 nm, polysilicon (150 nm) and borosilicate glass (BSG,

https://app.courseware.epfl.ch/learning/course/course-v1:EPFL+MICRO-621+2019/block-v1:EPFL+MICRO-621+2019+type@sequential+block@b01981a248d2425bba6e805fbd807f42/bl ock-v1:EPFL+MICRO-621+2019+type@vertical+block@b5ae443489d64b15ba9f9524d1fe9ff2

Photolithography

Dry etching

Wet etching

lift-off

Thermal evaporation

Sputtering

LPCVD

200 nm), are deposited on a silicon wafer (380 µm-thick double-sided-polished <100>- orientation) using LPCVD (Figure S2 - a). The wafer is then annealed at 1200°C for 15 minutes to dope the polysilicon layer via diffusion from the BSG. The techniques used are: The backside of the wafer is patterned via photolithography and dry etching to form alignment marks and a release pattern that will be later used to form silicon chips (Figure S2 -b). Next, the BSG layer is used to make a mask to define the piezoresistors: it is patterned by photolithography and then dry etched (Figure S2) - c). The polysilicon piezoresistors are defined in KOH 40% at room temperature. The BSG layer is then stripped in buffered HF (BHF, Figure S2 - d). Gold (Au, 190 nm) on chromium (Cr, 10 nm) metal traces are fabricated using lift-off photolithography and metal evaporation (Figure S2 - e). Finally, aluminum (Al, 200 nm) is deposited onto the bonding pads of the metal traces using another liftoff step (Figure S2 - f).

> S3-1-2 Single crystal silicon piezoresistor: In order to adapt the trilayer we will talk about cantilever process to integrate single crystal silicon piezoresistors the process one type of Si piezoresistors was modified to use Silicon-On-Insulator (SOI) technology where the buried SiO₂ layer functioned as the etch stop layer to protect the silicon piezoresistors during

the KOH etch. The boron doped single crystal silicon piezoresistors (BSG, diffusion at 1200°C for 15 minutes) were patterned through the silicon device layer of an SOI wafer (SOI 725-2-0.13) by photolithography and dry etching. The SOI wafer was initially mechanically ground from 725 µm to 380 µm to match its complementary wafer. LS-SiN was deposited by LPCVD as described in the section S3-1-1 and then punched (photolithography and dry etching) to make two openings for each piezoresistor. These openings acted as via to connect the metal contacts to the silicon piezoresistors. The gold metal contacts were then created by lift-off photolithography and metal evaporation. The BCB coating and bonding, and chip release were similar to the one with the polysilicon piezoresistors as illustrated in the manuscript. The buried SiO₂ was finally removed in diluted HF. For applications where the fluid/coating compatibility is required, a thin layer (ca. 20nm) of the oxide can be left by timing the HF process. This thin layer of SiO₂ does not compromise the functionality of the trilayer cantilevers because the tensile module of SiO₂ is relatively small compared to LS-SiN.

S3-2 Polymer addition

The trilayer structure is created by adhesive bonding two wafers. The adhesive used is a benzocyclobutene-based polymer (Cyclotene 3022-35, BCB). BCB is spin-coated onto the fabricated electronics (Figure S2 - g). A second wafer is

In the presentation

prepared with a LS-SiN layer (same LS-SiN thicknesses as the other wafer), and also coated with BCB. Then, both wafers are bonded in a vacuum bonder (max tool pressure 2500 mbar and max temperature 160 °C), and the bonded wafers were hard baked at 250°C for 1 hour (Figure S2 - h). The interface between both wafers forms the trilayer structure composed of BCB sandwiched between two LS-SiN films.

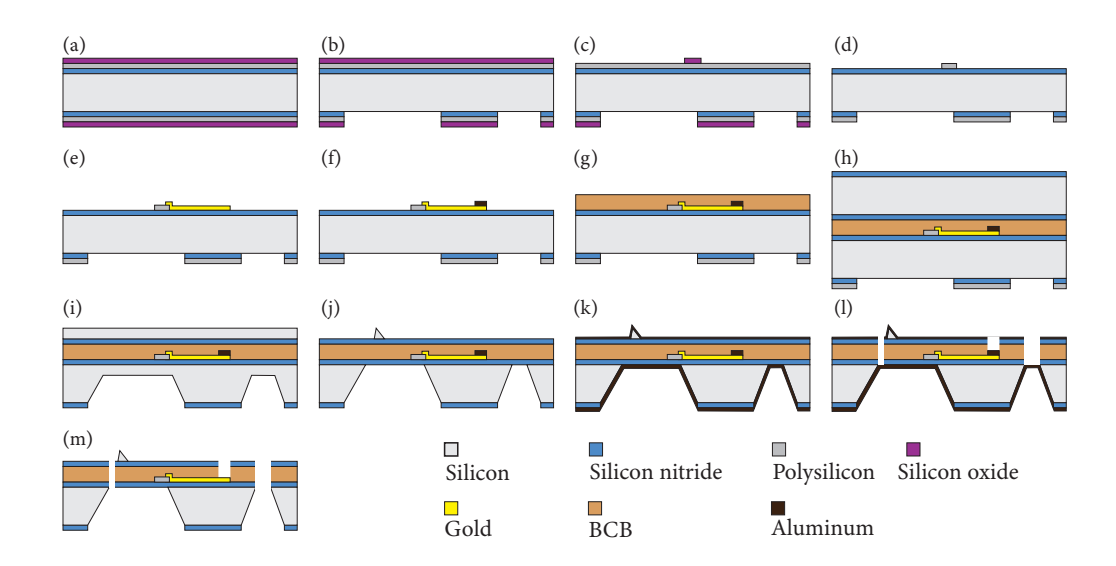


Figure S2. Tip-integrated trilayer AFM cantilever microfabrication process

S3-3 Silicon patterning

S3-3-1 Integrated silicon tips: Both silicon wafers are patterned: one to form chips for handling, the other to make sharp AFM silicon tips. The cantilever tips tips fabrication were patterned in two steps. First, the LS-SiN on the backside of the top wafer is blanket etched, then the silicon is wet-etched in KOH 40% at 60°C for roughly 15 hours, until a silicon layer of roughly 15 µm remains (Figure S2 - i). A pentagonal silicon dioxide (SiO₂) mask is fabricated using sputtering, lithography and dryetching. Finally, the wafer stack is immersed in KOH again to finish etching the silicon layer. The SiO₂ mask is under-etched and forms a sharp triangular pyramid tip on top of the trilayer membrane (Figure S2 - j).

S3-3-2 Integrated silicon nitride tips: Oxide sharpened² silicon nitride tips were created on the wafer with the sensing elements. Prior to the electronics integration (S3-1), the silicon wafer was covered with a 20 nm LS-SiN (LPCVD) film and circular openings were patterned by e-beam lithography and dry etching. LS-SiN was chosen over SiO₂ for its high etching resistance in KOH, making it a more suitable mask material to maximize tip sharpness. The tip molds were then created by silicon anisotropic KOH (40% at 60°C) etching. The LS-SiN mask was removed in 50% HF. This process differs from the integrated silicon tips in the

Here, we will talk

way that 400 nm of SiO_2 (for tip sharpening) was deposited prior to the LS-SiN structural layer. The rest of the process is like the recipe described above except that the 400 nm SiO_2 layer was removed in BHF after the cantilevers were released.

S3-4 Trilayer device patterning

The devices are patterned by dry-etching the trilayer membrane. To do so, aluminum is evaporated on both sides of the wafer (Figure S2 - k): on chip-side of the wafer for structural support (2 μ m), on the tip-side to fabricate a hard mask (400 nm). The cantilevers are then patterned with photolithography. The aluminum is first wet-etched, then the photoresist stripped. Finally, the trilayer membrane is dry-etched using fluorine chemistry (Figure S2 - k). To release the devices, the aluminum is wet-stripped (Figure S2 - l).

Note 4- Silicon tip sharpness assessment

To evaluate the tip sharpness, we imaged a polycrystalline titanium sample with the OBD method. The image was taken using a NanoScope-V controller and Multi-Mode-V AFM with a J scanner (Bruker) in tapping mode. To evaluate the tip sharpness, the blind tip estimation algorithm³, as implemented in the Gwyddion program^{4,5} has been used. The blind tip estimation algorithm is used to estimate the sharpness of the tip from the image of a polycrystalline titanium tip characterizer sample of unknown geometry, with features significantly sharper than the tip under evaluation. The Gwyddion partial blind tip estimation algorithm iterates over the surface of the image to find the high points with the steepest slopes on the image. These points are subsequently used to estimate the radius of the tip by taking the average width of the tip along the two orthogonal axes, using the assumption that the evaluated tip must be sharper than the sharpest feature on the image of the specimen. To guarantee that the dilation of the specimen surface results exclusively from the tip geometry, the noise suppression threshold is set at 100 pm, which is superior to the measured image noise of 40 pm. Additionally, the borders of the image are also excluded from the estimation to prevent edge artifacts. We took tapping mode images with 15 different cantilevers and the following imaging parameters: 2 μ m \times 2 μ m scan size, 1024×1024 pixels, and 2 Hz scan rate. The tips exhibited a radius of 17±2 nm at 10 nm below the apex (Figure S3).

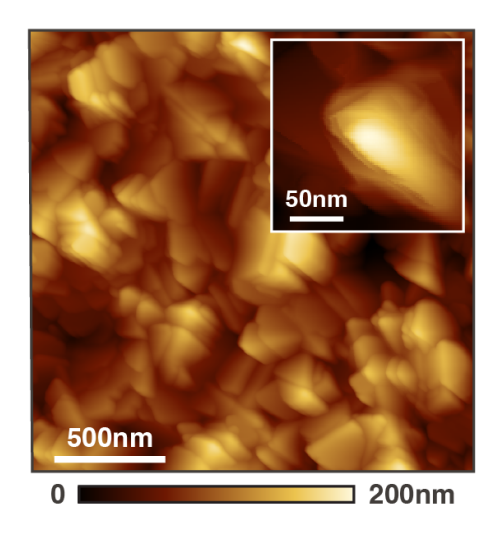


Figure S3. AFM image of a titanium polycrystalline roughness sample. The tip radius at 10 nm from the apex is estimated at 17 nm.

References

- 1- Fukuma, T. & Jarvis, S. P. Development of liquid-environment frequency modulation atomic force microscope with low noise deflection sensor for cantilevers of various dimensions. *Review of Scientific Instruments* 77, 043701 (2006).
- 2- Ravi, T. S., Marcus, R. B. & Liu, D. Oxidation sharpening of silicon tips. *J. Vac. Sci. Technol. B Microelectron. Nanometer Struct.* **9**, 2733 (1991).
- 3- Bykov, V., A. Gologanov, and V. Shevyakov. "Test structure for SPM tip shape deconvolution." *Applied Physics A Materials Science & Processing* 66, no. 5 (1998): 499-502.
- 4- Gwyddion Free SPM (AFM, SNOM/NSOM, STM, MFM, ...) data analysis software. http://gwyddion.net (accessed Oct 31, 2019).
- 5- Nečas, David, and Petr Klapetek. "Gwyddion: an open-source software for SPM data analysis." *Open Physics* 10, no. 1 (2012): 181-188.

Nickel etch video (Figure 4a) supplemented